Landscape Ecology

What are hot and what are not in an urban landscape: quantifying and explaining the land surface temperature pattern in Beijing, China

--Manuscript Draft--

Manuscript Number:	
Full Title:	What are hot and what are not in an urban landscape: quantifying and explaining the land surface temperature pattern in Beijing, China
Article Type:	Original research
Keywords:	Urban heat island, Urban structure, Land-use/land-cover, Heat fluxes, MODIS, Thermal infrared image
Corresponding Author:	Wenhui Kuang, Ph.D. Institute of Geographic Sciences and Natural Resources Research, Chinese Academy of Sciences Beijing, CHINA
Corresponding Author Secondary Information:	
Corresponding Author's Institution:	Institute of Geographic Sciences and Natural Resources Research, Chinese Academy of Sciences
Corresponding Author's Secondary Institution:	
First Author:	Wenhui Kuang, Ph.D.
First Author Secondary Information:	
Order of Authors:	Wenhui Kuang, Ph.D.
	Yue Liu, Ph.D.
	Yinyin Dou, M.M.
	Wenfeng Chi, M.M.
	Guangsheng Chen, Ph.D.
	Chengfeng Gao, M.M.
	Tianrong Yang, B.S.
	Jiyuan Liu, Ph.D.
	Renhua Zhang, Ph.D.
Order of Authors Secondary Information:	
Abstract:	Understanding how landscape components affect the urban heat island is crucial for urban ecological planning and sustainable development. This study was intended to quantify the spatial pattern of land surface temperatures (LSTs) and associated heat fluxes in relation to land-cover types in Beijing, China, using portable infrared thermometers, infrared thermal imagers, and Moderate Resolution Imaging Spectroradiometer. The spatial differences and the relationships between LST and the hierarchical landscape structure were analyzed with in situ observations of surface radiation and heat fluxes. Large LST differences were found among various land-use/land-cover types, urban structures, and building materials. Within the urban area, the mean LST of urban impervious surface area (UIS) was about 6-12 ℃ higher than that of the urban green space (UGS). LSTs of built-up areas were on average 3-6 ℃ higher than LSTs of rural areas. The surface radiation and heat fluxes observations indicated that the differences were caused by different fractions of sensible heat or latent heat flux in net radiation. Building materials and urban structure significantly influenced the spatial pattern of LST in the urban area. By contrast, elevation and vegetation cover are the major determinants of the LST pattern in the rural area. LST decreased with increasing elevation and Normalized Difference Vegetation Index. To

	alleviate urban heat island intensity in Beijing, urban planners and policy makers should pay special attention to selecting appropriate building materials, reasonably arranging urban structures, and designing rational landscape components.
Suggested Reviewers:	Dengsheng Lu dlu@indiana.edu
	Chi Zhang zc@ms.xjb.ac.cn
	Chunyang He hcy@bnu.edu.cn
	Jianguo Wu Jingle.Wu@asu.edu

Submit to *Landscape Ecology*

What are hot and what are not in an urban landscape: quantifying and explaining the land surface temperature pattern in Beijing, China

Wenhui Kuang • Yue Liu • Yinyin Dou • Wenfeng Chi • Guangsheng Chen • Chengfeng Gao • Tianrong Yang • Jiyuan Liu • Renhua Zhang

W. Kuang (Corresponding author) • Y. Liu • W. Chi • T. Yang • J. Liu • R. Zhang
Institute of Geographic Sciences and Natural Resources Research, Chinese Academy of Sciences, Beijing 100101, China
e-mail: kuangwh@igsnrr.ac.cn
phone: +86 1064888890/fax: +86 1064889276

Y. Dou
State Key Laboratory of Earth Surface Processes and Resource Ecology, Beijing Normal University, Beijing 100875, China

W. Chi
College of Resources and Environment, University of Chinese Academy of Sciences, 19A Yuquan Road, Shijingshan District, Beijing 100049, China

G. Chen
Environmental Sciences Division, Oak Ridge National Laboratory, Oak Ridge, TN 37831, USA

C. Gao
Southwest University of Science and Technology, Mianyang, China 621010

Date of the manuscript draft: June 30, 2014

Manuscript word count (title, abstract, keywords, body of text, figures, tables): 7300

Abstract

Understanding how landscape components affect the urban heat island is crucial for urban ecological planning and sustainable development. This study was intended to quantify the spatial pattern of land surface temperatures (LSTs) and associated heat fluxes in relation to land-cover types in Beijing, China, using portable infrared thermometers, infrared thermal imagers, and Moderate Resolution Imaging Spectroradiometer. The spatial differences and the relationships between LST and the hierarchical landscape structure were analyzed with in situ observations of surface radiation and heat fluxes. Large LST differences were found among various land-use/land-cover types, urban structures, and building materials. Within the urban area, the mean LST of urban impervious surface area (UIS) was about 6–12 ℃ higher than that of the urban green space (UGS). LSTs of built-up areas were on average 3–6 ℃ higher than LSTs of rural areas. The surface radiation and heat fluxes observations indicated that the differences were caused by different fractions of sensible heat or latent heat flux in net radiation. Building materials and urban structure significantly influenced the spatial pattern of LST in the urban area. By contrast, elevation and vegetation cover are the major determinants of the LST pattern in the rural area. LST decreased with increasing elevation and Normalized Difference Vegetation Index. To alleviate urban heat island intensity in Beijing, urban planners and policy makers should pay special attention to selecting appropriate building materials, reasonably arranging urban structures, and designing rational landscape components.

Keywords

Urban heat island, Urban structure, Land-use/land-cover, Heat fluxes, MODIS, Thermal

infrared image

Introduction

The alteration of an urban microclimate is often characterized by an urban heat island (UHI), which is defined as the phenomenon where atmospheric and land surface temperatures (LST) are higher in urban areas than in surrounding rural areas (Oke 1995; Voogt and Oke 2003). The UHI was regarded as the most prominent environmental issue in urban climate and cities' sustainable development (Oke 1984; Grimm et al. 2008; Alberti 2009; Wu 2010, 2013; Pickett et al. 2011). The UHI effect is mainly caused by the difference in surface physical properties, urban structure, land cover, land use, anthropogenic heat sources, air pollution, etc. (Oke 1982; Streutker 2003; Buyantuyev and Wu 2010). The land surface physical properties (e.g., albedo, emissivity, thermal capacity, thermal conductivity, thermal inertia) of various land-cover types (e.g., impervious surface, vegetation, water) are significantly different, which could result in LST heterogeneity. Indeed, the LST difference among various intra-urban land surfaces may be as large as, or even larger than, the urban-rural difference (Buyantuyev and Wu 2010). Accordingly, the complex intra-urban land surface variations in LST largely result from the different physical properties, including urban structure, which refers to the spatial dimensions of buildings and street canyons; urban land-cover, including impervious surfaces, green space, bare soil, and water; urban fabric, which refers to building materials; and urban metabolism, including anthropogenic sources of water, heat, and pollutants (Oke 2004). Understanding and quantifying UHI associated with a hierarchical landscape structure are important to improve the residential environment of urban dwellers (Wu 2010).

Urban landscape patterns, including landscape composition and configuration, is related

closely with LST (O'Neil et al. 1988; J. Li et al. 2011; Connors et al. 2013; Wu 2014). Landscape composition identifies the abundance and variety of land-cover types without considering their spatial characteristics, for example, the impacts of vegetation fraction and impervious surface area on LST (W. Zhou, Qian et al. 2011; Song et al. 2014). Cities are characterized by large fractions of impervious surfaces composed of concrete, asphalt, brick, pebbles or aggregates which absorb and store radiation during the daytime and slowly release heat during the night (Buyantuyev and Wu 2010). Furthermore, landscape composition influencing LST affects UHI directly by the modification of surface physical properties. The selections of building materials will greatly influence the land surface physical properties, such as albedo (Oke 1984). For example, lighter-colored building materials generally have higher albedo and absorb less heat, while darker materials generally absorb more heat than lighter materials and result in higher LST. Landscape configuration represents the spatial arrangement or distribution of land-cover features within landscape heterogeneity, and plays an important role in UHI due to the effect of surface fluxes. Therefore, it is crucial to consider both landscape composition and configuration used in urban design to mitigate the LST across urban areas (Wu 2010).

Currently, there are three major approaches for studying UHI: air temperature measurement from meteorological stations, LST retrieved from satellite remotely sensed images, and in situ observations of surface radiation temperature using portable infrared thermometers or infrared thermal imagers. The LST obtained from meteorological stations can reflect differences in atmospheric temperature over long periods; however, the extrapolation of the station data to region level is often biased by the distribution of the

meteorological stations (Oke 1982; Chen and Pan 1997; Ouyang et al. 2007; Yang et al. 2011). LST retrieved from remotely sensed products can be used to quantitatively represent spatial characteristics of LST at various urban surfaces, but it is limited by low temporal resolution and shorter data records (Dale and Jeffrey 1999; Ouyang et al. 2007) and difficulty in validating the retrieved results using ground-based measurements at different spatial scales (Mao et al. 2005; Ji et al. 2006; Y. Wang and Hu 2006). Ground-based measurements using infrared thermal instruments at a specific time and location can provide timely and accurate LST for specific land-use and land-cover types (X. Wang et al. 2011).

During the past two decades, a few studies addressed the phenomena of UHI or the relationship between landscape patterns and LST in Beijing. Based on Landsat Thematic Mapper (TM) images and a regression tree model, Xiao et al. (2007, 2008) estimated the spatial distribution of LST in Beijing and explored its relationship with the proportion of impervious surface. X. Li et al. (2012) revealed the relationship between the proportion of green space and LST based on Landsat TM images, and indicated that 10% increase in green space could result in 0.86 ℃ decrease in LST. Based on air temperature data from 20 weather stations during 41 years (1960–2000), Lin and Yu (2005) indicated that UHI intensity in Beijing had increased significantly with the accelerated urbanization, and the increasing trend of UHI intensity was 0.31 ℃/decade. Ji et al. (2006) estimated the impact of urban growth on UHI in Beijing based on MODIS LST products. In addition, the occurrence frequency of extreme high-temperature events in Beijing showed a significant increasing trend over the last decade (Chen and Pan 1997). The area of impervious surfaces is positively correlated with UHI, as proved by the fact that LST has increased by approximately 9.18 ℃

due to replacement of natural surfaces with impervious surfaces (Xiao et al. 2007). These studies suggest that LST in Beijing has significantly changed due to urbanization with increased impervious surfaces replacing natural vegetation.

Although several studies mentioned above addressed the spatial and temporal patterns of LST in Beijing, no studies have investigated the LST and surface energy fluxes for various landscape components. Through implementing the synchronized LST observations using portable infrared thermometers, infrared thermal imagers, and improved MODIS remotely sensed products, our specific objectives were to (1) quantify the LST and energy fluxes over various land-use/land-cover types, as well as building materials based on ground-based observations, (2) improve MODIS retrieval parameters to retrieve and estimate regional LST along an urban-rural gradient, and finally (3) assess the impacts of different land surface physical properties and urban structures on the magnitude and spatial distributions of LST.

Methods

Theories and measured scheme of LST

According to the surface energy budget equation, the net radiation (R_n) absorbed by a land surface (e.g., forest, crop, impervious surface area, water) is equal to the sum of incoming shortwave radiation (R_s) and longwave radiation ($L_\downarrow$) minus the reflected shortwave and emitted longwave radiation ($L_\uparrow$) (Equation 1).

$$R_n = (1-\alpha)R_s + L_\downarrow - L_\uparrow , \quad (1)$$

where, α is the surface albedo.

According to Stefan-Boltzmann's law, the energy emitted by an object per unit time and per unit area is determined by the materials of the body, the conditions of the land surface,

and LST, which can be expressed by the following formula:

$$L_{\uparrow} = \varepsilon \sigma T_s^{\,4}, \tag{2}$$

where ε is the land surface emissivity (LSE), σ is the Stefan-Boltzmann constant (5.67×10^{-8} $W\cdot m^{-2}\cdot K^{-4}$), and T_s is the radiometric LST (Z. Li et al. 2013). By integrating equations (1) and (2), the equation to calculate R_n is

$$R_n = (1-\alpha)R_s + \varepsilon L_{\downarrow} - \varepsilon \sigma T_s^{\,4}. \tag{3}$$

LST and LSE jointly determine $L_{\uparrow}$, while albedo determines R_s.

The net radiation can be further decomposed to sensible heat flux (H), latent heat flux (LE), and ground heat flux (G) .The relationship can be expressed as

$$R_n = LE + H + G. \tag{4}$$

In a bulk formulation, sensible heat flux can be assumed to be calculated as

$$H = \rho C_p (T_s - T_a)/r_{ae}, \tag{5}$$

where ρ (kg m^{-3}) and C_p (J kg^{-1} K^{-1}) are the density and specific heat of the moist air at the ground, T_s is the radiometric surface temperature (K), T_a is the air temperature at ground level (K), and r_{ae} (s m^{-1}) is the total resistance, given by the sum of the aerodynamic resistance and the additional resistance term that links radiometric and aerodynamic temperatures.

$$\lambda E = (\rho C_p/\gamma)(e_s - e_a)/r_{ae}\ , \tag{6}$$

where γ is the psychrometric constant, e_s is the saturated vapor pressure at a fictitious surface corresponding to that seen by the radiometer (r_{ae}) and e_a the vapour pressure of the air above the canopy.

From equations 1–6, we can find that the physical properties of a land surface (e.g.,

materials, surface roughness, albedo, emissivity) and the surrounding environmental conditions (e.g., canopy coverage, air temperature, elevation) could greatly influence the LST.

We aimed to explore LST of different land surfaces based on field observations and MODIS data. We adopted a synchronized approach by integrating remotely-sensed data with ground-based observations at local and regional scales. We measured LST of various land surfaces using the infrared thermal imager and portable infrared thermometer at multiple observation sites. With the ground-based observations, we calibrated the parameters of a MODIS LST algorithm and analyzed regional differences of LST for various land-use/land-cover types, urban building materials, and structures.

Ground-based measurements of LST

We used the portable infrared thermometer and infrared thermal imagers to measure LST. The portable infrared thermometer used in this study is the MAX4^{TM} produced by Raytek Inc. (Germany). For this instrument, the range of temperature measurement is -30–900 ℃, the measurement precision is ± 0.75% or 1 ℃, the response time is 250 ms, the spectral response is 8–14 μm, the optical resolution is 60:1, and the environmental temperature of operation is 0–50 ℃ (X. Wang et al. 2011). The infrared thermal imager used in this study is a Forward Looking Infrared Radiometer (FLIR) T425 model manufactured by FLIR Systems Inc. (USA). The field of view (FOV) of the device is 25°×19°/0.4 m, the thermal sensitivity is 0.05 ℃, the wavelength range is 7.5–13 μm, the infrared image resolution is 320×240 pixels, the temperature range is -20–1200 ℃, and the measurement precision is ± 2 %.

The portable infrared thermometer and infrared thermal imager were calibrated with a

standard calibration blackbody (BDB15, with a temperature precision of ± 0.1 ℃ and a resolution of 0.1 ℃) prior to the observations in order to eliminate the systematic error generated by the use of different instruments (X. Wang et al. 2011). To observe LST, the portable infrared thermometer MAX4^{TM} was placed far away from the observers. This device was placed at a height of 0.5 m above the object surface to measure the surface radiation temperature. We began to record temperatures after the devices became stable for 1–3 s. Continuous observations were made at all sites in the morning (LCT, 11:00–11:30) and at noon (LCT, 12:30–13:00). Ten observations were collected at each site during the study period, and the average values were calculated as the final temperature for this object. The infrared thermal imager FLIR T425 was installed 100 m above the ground. At this height, it can effectively observe the spatial characteristics of surrounding land surfaces. To preserve the measurement precision, the tilting angle of the imagers was less than 40^{o} and the maximum FOV distance was 2 km. Prior to measurement, the infrared thermal imager was calibrated using the LST measured by the portable infrared thermometers for the same objects. In the measured moment, the daily mean air temperature was 18–24 ℃, with 3 ℃ higher temperature at noon than in the morning. The air humidity was close to the long-term mean of 30% for Beijing, and the wind speed was lower than 2 m/s.

We selected four representative land-use/land-cover types to implement the LST measured experiments for urban-rural landscape components including UIS, UGS, farmland, and water body (Figure 1). The first selected zone (Z1) represented the UIS and UGS in the city, which is located around the Institute of Geographical Sciences and Natural Resources Research, Chinese Academy of Sciences, in Chaoyang District of Beijing. On the roof of a

100-m tall building in the Breezy Woods Oasis residential area, we installed an infrared thermal imager and a high-resolution camera to acquire infrared images for the surrounding buildings, the impervious surface area of a plaza, and green space in Olympic Park. Meanwhile, we also used the portable infrared thermometer to measure temperature at the ground surfaces of buildings, plaza, green space, and water bodies around this observation site. The second zone (Z2), which is located at the Beijing International Airport, was selected to represent a concrete land surface. Portable infrared thermometers were used to measure surface temperature of the airport tarmac. We selected the third zone (Z3) to represent farmland located in Xiaotangshan and the fourth zone (Z4) to represent the Miyun Reservoir water body.

#Figure 1 approximately here#

Ground-based measurements of surface radiation and heat fluxes

We also observed surface radiation and heat flux components for UIS, UGS, and farmland. We established stations S1 and S2 to observe radiation components and heat fluxes at UIS and UGS, respectively; they are located in the same zone (Z1) as the instrument for LST observation (Figure 1). The observation instruments at S1 and S2 were installed at 2.5 m and 1.6 m above the ground, respectively. Within the 1-km buffer zones of the two observation sites, the major land-cover types are impervious surface and vegetation. The UIS of the station S1 account for 71% in the buffer zone, and the vegetation of station S2 account for 78% in the buffer zone. In addition, we also established station S3 to collect data for farmland in Daxing District (Figure 1) (S. Liu et al. 2013). The observation instrument is installed at 3.0 m above the ground at this site. The instruments for measuring radiation and surface heat

fluxes include a three-dimensional ultrasonic anemometer (CSAT3), a humidity and temperature sensor (HMP155), a 4-Component Net Radiation Sensor (HFP01), and a soil heat flux sensor. The observation variables include upwelling and downwelling short-wave/long-wave radiation, albedo, land surface net radiation, sensible heat flux, latent heat flux, soil heat flux, and radiation temperature. For analysis, we first selected all the observation data during daytime (i.e., net radiation flux > 0) and removed the hard spikes and soft spikes. The data were further corrected using time-lagging, ultrasonic virtual temperature and air density (WPL correction) methods (Webb et al. 1980). Finally, the sensible and latent fluxes were corrected using the Bowen ratio energy balance closure method (Twine et al. 2000). We obtained the land surface radiation and energy fluxes for impervious surface area, urban green space, and rural farmland during the time when the MODIS satellite passed over the observation sites between 11:00 and 11:30 AM (LCT).

MODIS-based observations and parameterization

On September 20, 2011, the Terra MODIS satellite passed the observation sites at 11:10 AM (LCT) with a solar angle of 40.37°–41.84°. Two datasets from MODIS products were used to retrieve LST: (1) the 250-m spatial resolution MODIS 1B products and the 1-km resolution brightness data from the infrared thermal bands 31 (10.78–11.28 μm) and 32 (11.77–12.27 μm). The brightness can be calculated as

$$T_i = \frac{C_2}{\lambda ln(1+C_1/\lambda_i^5 R_i)} \quad , \tag{7}$$

where T_i is the brightness of bands 31 and 32, i is the band number (31 or 32), R_i is the radiance at the top atmosphere of band i, λ_i is the effective wavelength, C_1 and C_2 are constants C_1=1.19104×10^8 W·μm^4·m^{-2}·sr^{-1} and C_2= 1.43887×10^4μm·K (J. Zhou et al. 2009).

The parameters (e.g., C_1 and C_2) are derived from either empirical knowledge or regression analysis in terms of the natural land surfaces. Split-window algorithms were first introduced by Becker and Li (1995), and then Mao et al. (2005) and Wan et al. (2002) further developed two generalized split-window algorithms for LST retrieval based on MODIS data. Subsequent studies indicated that the Mao et al. (2005) retrieval algorithm was better than other algorithms for retrieving LST based on MODIS data (e.g., J. Zhou et al. 2009); therefore, we will apply the Mao et al. (2005) algorithm to retrieve LST in this study. We calculated the specific emissivity based on the 30 m × 30 m Landsat TM and Enhanced Thematic Mapper Plus (ETM+) land-use/land-cover information and 1-km resolution data for the fractions of impervious surface area and green space (J. Liu et al. 2010).

The Mao et al. (2005) retrieval algorithm is listed as follows:

$$T_S = \alpha(C_{32} (B_{31} + D_{31}) - C_{31}(D_{32} + B_{32}))/(C_{32} A_{31} - C_{31} A_{32}) + \beta, \quad (8)$$

where T_S is the LST and α and β are the fitted regression parameters for surface temperature between ground-based and remote - sensing observations, which were set as 0.7554 and 7.5146, respectively, in this study. A_{31}, A_{32}, B_{31}, B_{32}, C_{31}, C_{32}, D_{31}, and D_{32} are the parameters determined by multiple factors such as atmospheric transmittance and surface albedo (Mao et al. 2005).

We used the mean LST measured from ground-based observations during 10 minutes between 11:00 and 11:20 AM (LCT) when the MODIS satellite passed over the observation sites to recalibrate the parameters for different land surfaces (both mixed and pure pixels). In the urban area, most of the land surfaces are impervious, green space, and water. By multiplying the LST and the fractions of each surface type within a MODIS pixel (i.e., 1 km

× 1 km), we calculated the mean LST of this mixed pixel. The LST for each land-surface type in a pixel were derived from the infrared thermal imagers and portable infrared thermometers. Totally, we obtained 15 samples (or MODIS pixels) for calibrating the parameters for the Mao et al. (2005) algorithm. Finally, the parameters α and β in Equation (8) were determined as 0.7554 and 7.5146, respectively. Based on the calibrated parameters, the mean standard error was less than 2 ℃ and the root-mean-square error was 1.42 ℃ between the improved Mao et al. (2005) retrieval algorithm and observed LST (Figure 2).

#Figure 2 approximately here#

Analysis methods

The analysis of the LST along an urban-rural gradient was organized at four levels (Figure 3): observation objects (i.e., urban land, rural land), land-cover types, land-use types, and urban structures and materials (Wu and David 2002). The analysis of LST for various land surfaces was based on both ground-based observations and MODIS retrieval, whereas the regional LST was based on the MODIS retrieval LST derived from the calibrated Mao et al. (2005) algorithm.

#Figure 3 approximately here#

The LST difference among various land surfaces is calculated as:

$$\Delta T_{i,j,\mathrm{n}} = \frac{T_{i,n}\varepsilon_{i,n}}{0.95} - \frac{T_{j,n}\varepsilon_{j,n}}{0.95} \quad , \tag{9}$$

where $\Delta T_{i,j}$ is the LST difference between i and j land surfaces, T_i and T_j are LSTs of i and j land surfaces, respectively, n is the observation time period, and ε_i and ε_j are the specific emissivities for i and j land surfaces at the wavelength between 8 and 14 μm. For

different observation periods and different land surfaces, the specific emissivities are different (Table 1).

Table 1 approximately here#

The statistical analyses were conducted using SPSS 16.0. We used one-way analysis of variance (ANOVA) and F-test to quantify the relationships between LST and land surfaces and identify the sources of errors. The LST differences among different land uses, land covers, and building materials were tested and considered significant at a confidence level of 95% ($\alpha = 0.05$) unless specifically stated otherwise. The Pearson correlation was conducted to evaluate the correlation among the Normalized Difference Vegetation Index (NDVI), elevation (digital elevation model), and LST.

Auxiliary data

Several auxiliary datasets were used to identify the causes of LST differences for various land surfaces at regional scale, including 2010 Landsat TM/ETM+ land-cover/land-use data (30-m spatial resolution) (J. Liu et al. 2010; Kuang et al. 2013), 2010 aerial photos of Beijing (spatial resolution 0.5 m), SRTM elevation data (spatial resolution 90 m), and MODIS NDVI data (spatial resolution 1 km).

Results and analysis

Observed LST of various urban land surfaces

Using portable infrared thermometers and infrared thermal imagers to obtain ground-based observation points (n = 2250), we compared the LST for different land-use/land-cover types. In the morning (LCT, 11:00–11:30 am), the highest LST was measured on the building roof (36.80 ℃), followed by the airport tarmac (30.65 ℃), paved roads (30.03 ℃), plaza

(28.30 ℃), and green space (24.14 ℃), and the lowest was recorded for the water body (11.87 ℃, Figure 4). The LSTs for various green-space types were ranked as roadside green space (25.32 ℃) > residential green space (24.76 ℃) > park green space (22.34 ℃). Buildings, plaza, and paved roads showed strong "hot fields," while the green spaces acted as obvious "cold fields." At daytime, the LSTs of impervious surface areas (including building roof, airport tarmac, paved roads, and plaza) ranged 30–39 ℃, while green spaces ranged 24–27 ℃, with a difference of 6–12 ℃ between these two land-use types. The maximum difference between the building roof and water body was 24.92 ℃. In addition, we also found large variations among the measurements for a specific land-use type. For example, the LST difference was 29 ℃ between the maximum and minimum measurements for the building roof. The variations among measurements for three green-space types ranged 6–14 ℃, with lower variations in the park green space. The smallest variation occurred at the water body (4 ℃) due to its high thermal inertia and thermal capacity, and relatively low thermal conductivity. Using infrared thermal imagers to obtain the radiative temperatures distribution, we found the spatial heterogeneities of radiative temperatures were strong (Figure 5). In the urban area, green spaces had very low radiative temperatures in contrast to the roads and the roofs of buildings, and the roofs were the hottest surface in the morning. The radiative temperatures were significantly different for the same types of buildings with various materials and facades. For instance, the radiative temperatures of the roof and side facade of a building were around 49 ℃ and 46 ℃, respectively, although they were made of the same materials.

#Figure 4 approximately here#

Figure 5 approximately here#

LST difference between urban and rural areas

Based on the MODIS-retrieved LST and land-use/land-cover maps, we analyzed the LST of various land-use/land-cover types in the urban and rural areas of Beijing. Various land-use components in the urban and rural areas exhibited significantly different LSTs, with a descending order of the urban impervious surface area > rural residential area > cropland > grassland > forest > water body (Figure 6). The highest LST was distributed primarily in the urban and rural residential areas, where the major land-use component was construction, with a mean LST of 29.33 ℃. The mean LST of the urban impervious surface area was about 2 ℃ higher than that of the farmland, which is primarily located around the residential areas in eastern and northern Beijing, such as Shunyi District, Tongzhou District, and Daxing District (Figure 1). LST of grassland (24.48 ℃) was slightly higher than that of forest (22.85 ℃). A lower LST (21.52 ℃) was primarily located in the northern and western mountainous region, which was about 8 ℃ lower than LSTs in the urban and rural residential areas (Figure 2). The water body had the lowest LST (16.35 ℃). Thus, LST in the area surrounding Miyun Reservoir was lower than the northern and western mountainous region. The LST patterns of different land-use types retrieved from improved MODIS algorithms were consistent with that from the ground-based observations using the portable infrared thermometer and infrared thermal imager.

#Figure 6 approximately here#

Overall, our results indicated that LST of the urban area was about 3–6 ℃ higher than that of the rural area. The LST generally descended with increasing distance from the center

of urban. The districts closer to the urban area, such as Dongcheng, Xicheng, Haidian, Chaoyang, Shijingshan, and Fengtai districts, generally had higher LST (29.51 ℃) than those in the suburban area (28.79 ℃), such as Daxing, Tongzhou, Fangshan, Mentougou, Changping and Shunyi districts. The rural areas, such as Huairou District, Pinggu District, Yanqing County, and Miyun County, had an even lower LST (28.07 ℃). For grassland and forest, the LSTs in the urban were about 3 ℃ and 2 ℃ higher, respectively, than in the suburban area, and the differences between suburban area and rural area were smaller. For water bodies, the LST in the urban was about 3 ℃ and 6 ℃ higher than in the suburban area and rural area, respectively.

Land surface radiation and energy fluxes of different land-use types

Except for the land surface physical properties and other climatic and atmospheric conditions, radiation and energy fluxes play a major role in the difference in LST for various land surfaces. Therefore, we specifically observed the net radiation, four radiation components, and the energy fluxes during 11:00–11:30 AM (LCT) and daytime (i.e., solar radiation > 0) on September 20, 2011, at the selected sites S1, S2, and S3 (Tables 2 and 3). The downwelling short-wave radiation was higher than 700 W/m^2 for all three observation sites during 11:00–11:30 AM (LCT) (Table 2). The upwelling long-wave radiation was higher than 400 W/m^2 during 11:00–11:30 AM (LCT), which was comparable with the daytime observations. Rural farmland had the highest net radiation, and the impervious surface had the lowest at 396.07 W/m^2.

Table 2 approximately here#

The land surface reflectance of different land-use types were ranked as impervious

surface area > urban green space > rural farmland (Table 3). The impervious surface area had the highest reflectance and the lowest net radiation. In contrast, urban green space and farmland had higher net radiations but lower reflectances. The fractions of sensible heat in net radiation (H/Rn) ranked as impervious surface > urban green space > rural farmland, and the fractions of latent heat (LE/Rn) showed an opposite pattern. The H/Rn ratio was about 0.63 and the LE/Rn ratio was 0.19 for the UIS area. The radiation energy at the impervious surface was primarily composed of sensible heat, with a Bowen ratio (H/LE) of 4.03. For urban green space, latent heat fraction (0.58) was higher than sensible heat (0.32) because of vegetation transpiration. For rural farmland, the lowest reflectance (0.14) resulted in the highest net radiation. Similar to green space, the high plant transpiration in farmland caused higher latent heat fraction (0.63) than sensible heat fraction (0.30). Sensible heat flux dominated the energy balance at the impervious surface, resulting in higher LST; latent heat flux played the major role in the energy balance of green space and farmland, resulting in lower LST compared to impervious surface. From these analyses, we concluded that the difference in LST among various land-use types was primarily determined by the significantly different energy balance.

#Table 3 approximately here#

The effects of topography and vegetation coverage on LST

LST is not only influenced by land-use/land-cover types, but also by elevation, vegetation coverage, local meteorological condition, urban land fraction, and human population density. Therefore, even for the same land-use type, the mean LST may be different in different locations along the urban-rural gradient. We overlaid the retrieved MODIS LST with

elevation and vegetation cover (represented by NDVI) to find the relationships between LST and elevation and vegetation cover (Figure 7). Beijing is located in northern North China Plain, with a mountainous terrain (the elevation between 1,000m and 1,500 m) in the northwest and a flat plain (the elevation between 0m and100 m) in the southeast. The mean LST in the northwest was 19.65 ℃, ranging between 14.14 ℃ and 24.08 ℃; the mean LST in the southeast was 28.15 ℃, ranging between 23.87 ℃ and 32.82 ℃. We found that LST decreased significantly with increasing elevation (Figure 7; $R^2 = 0.80$; $p < 0.01$). The LST in the west, which has more vegetation cover, was lower than that in the east, which has less vegetation cover. Statistical analyses indicated that LST first increased with NDVI when NDVI <= 2.0, then slightly decreased with NDVI when 2.0 < NDVI < 4.5, and greatly decreased when NDVI >= 4.5 (Figure 7). This pattern reflected an urban-rural gradient of NDVI: low NDVI values in the inner city (mostly construction land), relatively high NDVI in the suburban area (mostly residential and farmland area), and the highest NDVI in the rural area (mostly forest).

#Figure 7 approximately here#

Effects of landscape components and building materials on LST

Within the urban area, LSTs are closely related to the combination of multiple land-use types and building materials. The urban land surface primarily consists of three major landscape components: impervious surface, green space, and water. Based on the three observation approaches of direct measurements, infrared thermal imagers, and portable infrared thermometers, we found that the LSTs among these three land-cover types were significantly different, with a mean LST 6–12 ℃ higher at the impervious surface than that at the green

space. Therefore, the fractions of each land-cover component may determine the overall LST. In addition, we found that building materials, shapes, colors, and shadows significantly influenced the infrared images and thus LST. For example, the LST of a dark-gray roof was about 4.8 ℃ higher than that of a white-gray roof due to the higher energy absorption capacity of dark-gray materials. The LST of a concrete plaza in the shadow of tall buildings was about 10 ℃ lower than that of a concrete plaza without shadow. LST of an asphalt road was about 2 ℃ higher than that of a concrete road because the lighter color of the concrete has a higher reflectance and lower absorption to solar radiation. The building roof was directly exposed to solar radiation, so its LST was significantly higher than that of the lateral building walls. Therefore, the building materials with higher heat adsorption capacity should contribute more to the formation of UHIs. The different impacts of building materials were primarily reflected in their differences in thermal conductivity, reflectance, and thermal inertia. The buildings, roads, and plazas are generally made of bricks, tiles, concrete, and asphalt. Although these materials have high reflectance to solar radiation, they also have faster heat transfer and higher heat-trapping capacity. These characteristics make the built-up land in the urban the highest LST compared to other land-cover types or locations along the urban-rural gradient. The green space with grass and trees has high vegetation evapotranspiration. Therefore, the thermal inertia and the resistance to rising surface temperature were very large, resulting in significantly lower LST than the impervious surface.

Discussion

Effects of urbanization on LST in Beijing

Urbanization, the process of converting natural vegetation and cropland to urban impervious surfaces, was a major force of land-use/land-cover change. The LST as an important parameter in studying UHI is primarily related to the altered landscape structure due to rapid urbanization. For instance, urban areas covered with impervious surfaces such as buildings, asphalt, concrete, etc. generally have higher absorption of solar radiation and larger thermal conductivity and capacity, which may result in a relatively higher temperature compared to the surrounding rural areas. The land-cover type (such as vegetation or impervious materials) and spatial composition in the landscapes are also important in determining both internal and external urban LSTs (Rosenzweig et al. 2005; W. Zhou, Huang et al. 2011). Furthermore, the spatial heterogeneity of landscapes may represent the larger intra-urban differences in LST (Buyantuyev and Wu 2010). Using the ground-based observations and the MODIS remotely-sensed products, we found that the LSTs of various land surfaces followed an order of UIS > UGS > water body. This implies that the higher fractions of impervious surface create higher LST in the urban. Notably, our study, based on in-situ measurements using infrared thermal imagers, quantitatively proved the spatial heterogeneities of LST in the urban area were strong. Beijing has experienced fast urban expansion in the past three decades, with more than a threefold increase in built-up area since 1984 (Kuang 2012b), which resulted in an increase of UHI by 0.31 ℃ /decade from 1960 to 2000 (Lin and Yu 2005). By the end of 2010, 19.62 million people lived in the city, and the population density was 1,195 persons km^{-2}. Its total area was 16,801 km^2, with 1,582.24 km^2 of impervious surface covering 72.6%

of the built-up area (Kuang 2011, 2012a; Kuang et al. 2013). Yu et al. (2005) indicated the increasing UIS area in Beijing resulted in an increase of LST by 9.18℃, although the increasing air temperature partly contributed to this. Our analysis for the relationship between NDVI and LST also proved that LST significantly decreased with increasing NDVI (Figure 7). Increases of UGS fraction in the urban area could reduce the increasing trend of LST (Weng et al. 2004; Buyantuyev and Wu 2010; X. Li et al. 2012). We found the urban landscape cover components (e.g., impervious surface or green space) are the most important key factors related to LST. Therefore administrators of the Beijing megacity should appropriately consider increasing the proportion of green space in urban and suburb areas to mitigate the UHI.

LST and land surface energy fluxes

LST plays a key role in controlling the land surface energy budget (Weng et al. 2013). In turn, the surface energy balance is an essential element of the climate system, and the land surface energy budget can be used to explain the changes of LST. Bare soil and vegetated surfaces have a high evapotranspiration potential and can release a relatively large amount of their absorbed energy as latent heat, resulting in a low LST. In addition, soil and vegetated surfaces have higher thermal conductivity than impervious surfaces and tend to store more of the absorbed energy, thus releasing less energy to the air, resulting in a low LST (Hafner and Kidder 1999; Hawkins et al. 2004). In contrast, urban impervious surfaces have higher absorption of solar radiation and higher thermal conductivity and capacity, and thus tend to absorb more incident solar energy and release their absorbed energy as sensible heat to the air, especially during night time, resulting in higher surrounding temperature. So the green space

in an urban area is generally an "urban heat sink" (Carnahan and Larson 1990), whereas the impervious surfaces are "urban heat sources". In this study, we found that the components of net radiation (i.e., latent heat, sensible heat, and conduction heat fluxes) over various land-cover types were significantly different. These differences may explain the higher LST in the urban impervious surface areas than in the green space and farmland areas. Based on ASTER remotely-sensed data, Weng et al. (2013) found the net radiation of various land-cover types followed an order of farmland > UGS > UIS, which is consistent with our study (Table 2 and 3).

LST and building materials

Besides microclimatic conditions (e.g., air temperature, precipitation, and cloud cover), land use, urban structure, and anthropogenic heat sources (Oke 1982), the thermal dynamics in an urban area are also significantly influenced by building materials (Meyn and Oke 2009). The influences of building materials on LST are reflected primarily in differences of the physical properties of materials (e.g., thermal conductivity, reflectance, albedo, and thermal capacity). For example, lighter-colored building materials generally have higher albedo and absorb less heat, while darker materials generally absorb more heat, resulting in higher LST at the darker-material surfaces. A rough land surface often absorbs more heat as the surface area is higher, thus larger, than smooth land surfaces (Doulos et al. 2004). In addition, the LST of concrete pavements is generally lower than asphalt surfaces (Asaeda et al. 1996). An earlier report indicated that the building materials of old bricks and tiles within the second ring of Beijing had lower reflectance, creating an extremely high LST (W. Liu et al. 2011). X. Wang et al. (2003) found that the surface roughness of the inner city in Beijing is about an order of

magnitude higher than that of the suburban area due to many tall buildings, which resulted in significant changes in the thermal dynamics (Xu et al. 2009). In this study, we found that LSTs of dark-colored land surfaces and asphalt roads were significantly higher by 4.8 ℃ and 2℃, respectively, than white-colored surfaces and concrete roads. The building roof had a higher LST than the lateral building walls, and the areas in building shadows had a lower LST by 9.9 ℃ than those without shadows. Therefore, we suggest that the city planners and designers should select building materials with higher albedo and low thermal capacity and rationally arrange land-use components in the urban areas.

Conclusions

LST varied significantly along the urban-rural gradient, which is not only resulted from the differences in solar radiation but also from the differences in atmospheric environment and land surface characteristics. The integration of ground-based observations with remotely-sensed retrieval was proved effective to explore the spatial and temporal characteristics of LST along an urban-rural gradient from the perspectives of land-cover type, land-use types, urban structure, and building materials. The portable infrared thermometer and infrared thermal imagers can observe the LST difference at local scale for different building materials and provide parameterization and validation data for MODIS retrieval at medium scale. The improved MODIS retrieval algorithms reduced the mean error to 2 ℃ as compared to the observed LST.

The LST was significantly different between urban and rural land surfaces, with about 3–6 ℃ higher in the urban area than in the rural area. Large differences were also found among various intra-urban land-use types (i.e., impervious surface, green space, and water),

with about 6–12 ℃ higher at the impervious surface than at the green space. Our results indicate that the different LSTs in the urban area were primarily caused by the differences in land surface radiation and energy fluxes. Sensible heat flux is the major component of net radiation for an impervious surface and thus resulted in increased LST, whereas latent heat flux is the major component of net radiation for green space.

LST is also significantly influenced by urban structure and building materials in built-up areas, and elevation and vegetation cover in rural area. We found that LST decreased with increasing elevation and NDVI. The concrete land surfaces had lower LST than that of asphalt surfaces, and dark-gray buildings had higher LST than white-gray buildings. To alleviate UHI intensity in Beijing, the city planners and designers should pay special attention to selecting appropriate building materials, reasonably arranging urban structures, increasing green space fractions, and designing rational landscape components.

Acknowledgements

We thank the National Natural Science Foundation of China (41371408), the National Basic Research Program of China (2014CB954302; 2010CB950900), and National Key Technology R&D Program (2012BAJ15B02) for financial support. We also thank Prof. Shaomin Liu of Beijing Normal University for providing the radiation and energy fluxes data from the Daxing Station. We thank Prof. Jianguo Wu to improve the manuscript.

References

Alberti M (2009) Advances in urban ecology: integrating humans and ecological processes in urban ecosystems. Springer, New York

Asaeda T, Ca VT, Wake A (1996) Heat storage of pavement and its effects on the lower atmosphere. Atmos Environ 30(3):413–427

Becker F, Li ZL (1995) Surface temperature and emissivity at various scales: definition, measurements and related problems. Remote Sens Rev 12:225–253

Buyantuyev A, Wu JG (2010) Urban heat islands and landscape heterogeneity: linking spatiotemporal variations in surface temperatures to land-cover and socioeconomic patterns. Landscape Ecol 25(1):17–33

Carnahan WH, Larson RC (1990) An analysis of an urban heat sink. Remote Sens Environ 33:65–71

Chen SB, Pan LQ (1997) Effects of urbanization on the annual mean temperature of Beijing. Acta Geogr Sin 52(1):27–36

Connors JP, Galletti CS, Chow W (2013) Landscape configuration and urban heat island effects: assessing the relationship between landscape characteristics and land surface temperature in Phoenix, Arizona. Landscape Ecol 28(2):271–283

Dale A, Jeffrey C (1999) Thermal infrared remote sensing for analysis of landscape ecological processes: methods and applications. Landscape Ecol 14:577–598

Doulos L, Santamouris M, Livada I (2004) Passive cooling of outdoor urban spaces: the role of materials. Sol Energy 77(2):231–249

Grimm NB, Faeth SH, Golubiewski NE et al (2008) Global change and the ecology of cities.

Science 319(5864):756–760

Hafner J, Kidder SQ (1999) Urban heat island effect modeling in conjunction with satellite-derived surface/soil parameters. J Appl Meteorol 38(4):448–465

Hawkins TW, Brazel AJ, Stefanov WL et al (2004) The role of rural variability in urban heat island determination for Phoenix, Arizona. J Appl Meteorol 43(3):476–486

Humes KS, Kustas WP, Moran MS et al (1994) Variability of emissivity and surface temperature over a sparsely vegetated surface. Water Resour Res 30(5):1299–1310

Ji CP, Liu WD, Xuan CY (2006) Impact of urban growth on the heat island in Beijing. Chinese J Geophys-ch 49(1):69–77

Kuang WH (2011) Simulating dynamic urban expansion at regional scale in Beijing-Tianjin-Tangshan Metropolitan Area. J Geogr Sci 21(2):317–330

Kuang WH (2012a) Evaluating impervious surface growth and its impacts on water environment in Beijing-Tianjin-Tangshan Metropolitan Area. J Geogr Sci 22(3):535–547

Kuang WH (2012b) Spatio-temporal patterns of intra-urban land use change in Beijing, China between 1984 and 2008. Chinese Geogr Sci 22(2):210–220

Kuang WH, Liu JY, Zhang ZX et al (2013) Spatiotemporal dynamics of impervious surface areas across China during the early 21st century. Chinese Sci Bull 58(14):1691–1701

Labed J, Stoll M P (1991) Spatial variability of land surface emissivity in the thermal infrared band: spectral signature and effective surface temperature. Remote Sens Environ 38(1):1–17

Li JX, Song CH, Cao L et al (2011) Impacts of landscape structure on surface urban heat islands: a case study of Shanghai, China. Remote Sens Environ 115:3249–3263

Li XM, Zhou W, Ouyang Z et al (2012) Spatial pattern of green space affects land surface temperature: evidence from the heavily urbanized Beijing metropolitan area, China. Landscape Ecol 27(6):887–898

Li ZL, Tang BH, Wu H et al (2013) Satellite-derived land surface temperature: current status and perspectives. Remote Sens Environ 131:14–37

Lin XC, Yu SQ (2005) Interdecadal changes of temperature in the Beijing region and its heat island effect. Chinese J Geophys-ch 48:47–54

Liu JY, Zhang ZX, Xu XL et al (2010) Spatial patterns and driving forces of land use change in China during the early 21st century. J Geogr Sci 20:483–494

Liu SM, Xu ZW, Zhu ZL et al (2013) Measurements of evapotranspiration from eddy-covariance systems and large aperture scintillometers in the Hai River Basin, China. J Hydrol 487:24–38

Liu WY, Gong AD, Zhou J et al (2011) Investigation on relationships between urban building materials and land surface temperature through a multi-resource remote sensing approach. Remote Sens Inform 4:46–53

Mao KB, Qin ZH, Shi J et al (2005) A practical split-window algorithm for retrieving land surface temperature from MODIS data. Int J Remote Sens 26(15):3181–3204

Meyn SK, Oke TR (2009) Heat fluxes through roofs and their relevance to estimates of urban heat storage. Energ Buildings 41(7):745–752

Oke TR (1982) The energetic basis of the urban heat island. Q J Roy Meteor Soc 108:1–24

Oke TR (1984) Methods in urban climatology. In: Kirchhofer W, Ohmura A, Wanner H (eds) Applied Climatology, Zürcher Geogr. Schriften 14:19–29

Oke TR (1995) The heat island of the urban boundary layer: characteristics, causes and effects. In: Cermak JE, Davenport AG, Plate EJ et al (eds) Wind climate in cities: Proceedings of the NATO Advanced Study Institute, Waldbronn, Germany, July 5–16, 1993. Nato Science Series E, vol 277. Kluwer Academic Publishers, Dordrecht, pp 81–107

Oke TR (2004) Initial guidance to obtain representative meteorological observations at urban sites. Instruments and Observing Methods Report No 81. World Meteorological Organization, Geneva

O'Neill RV, Krummel JR, Gardner RH et al (1988) Indices of landscape pattern. Landscape Ecol 1:153–162

Ouyang Z, Xiao RB, Schienke EW et al (2007) Chapter 27: Beijing urban spatial distribution and resulting impacts on heat islands. In: Hong K, Nakagoshi N, Fu BJ et al (eds) Landscape ecological applications in man-influenced areas: linking man and nature systems. Springer, New York, pp 459–478

Pickett STA, Cadenasso ML, Grove JM et al (2011) Urban ecological systems: scientific foundations and a decade of progress. J Environ Manage 92:331–362

Qin Z, Li W, Xu B et al (2004) The estimation of land surface emissivity for Landsat TM6. Remote Sens Land & Resour 3:28–32

Rosenzweig C, Solecki W, Parshall L et al (2005) Characterizing the urban heat island in current and future climates in New Jersey. Global Environ Change B 6:51–62

Song J, Du S, Feng X et al (2014) The relationships between landscape compositions and land surface temperature: quantifying their resolution sensitivity with spatial regression

models. Landscape Urban Plan 123:145–157

Streutker DR (2003) Satellite-measured growth of the urban heat island of Houston, Texas. Remote Sens Environ 85:282–289

Twine TE, Kustas WP, Norman JM et al (2000) Correcting eddy-covariance flux underestimates over grassland. Agric For Meteorol 103:279–300

Voogt JA, Oke TR (2003) Thermal remote sensing of urban climates. Remote Sens Environ 86:370–384

Wan ZM, Zhang YL, Zhang QC et al (2002) Validation of the land-surface temperature products retrieved from Terra Moderate Resolution Imaging Spectroradiometer data. Remote Sens Environ 83:163–180

Wang X, Bian LG, Lu CG (2003) A study of characteristic parameters of atmospheric boundary layer over Beijing in urban and suburban area in Autumn. Clim Environ Res 8(4):475–484

Wang XX, Hu DS, Zhu QJ (2011) Comparison of infrared radiative temperatures from two scales on different land surfaces. Journal of Guangxi Normal University 29(2):1-4 (in Chinese)

Wang Y, Hu F (2006) Variations of the urban heat island in summer of the recent 10 years over Beijing and its environment effect. Chinese J Geophys-ch 49(1):61–68

Webb EK, Pearman GI, Leuning R (1980) Correction of flux measurements for density effects due to heat and water vapour transfer. Q J R Meteorol Soc 106:85–100

Weng Q, Hu X, Quattrochi DA et al (2013) Assessing intra-urban surface energy fluxes using remotely sensed ASTER imagery and routine meteorological data: a case study in

Indianapolis, U.S.A. IEEE J Sel Top Appl PP(99):1–12

Weng Q, Lu D, Schubring J (2004) Estimation of land surface temperature–vegetation abundance relationship for urban heat island studies. Remote Sens Environ 89(4):467–483

Wu JG (2010) Urban sustainability: an inevitable goal of landscape research. Landscape Ecol 25:1–4

Wu J (2013) Landscape sustainability science: ecosystem services and human well-being in changing landscape. Landscape Ecol 28:999–1023

Wu J (2014) Urban ecology and sustainability: the state-of-the-science and future directions. Landscape Urban Plan, doi: http://dx.doi.org/10.1016/j.landurbplan.2014.01.018

Wu JG, David JL (2002) A spatially explicit hierarchical approach to modeling complex ecological systems: theory and applications. Ecol Model 153(1):7–26

Xiao R, Ouyang Z, Zheng H et al (2007) Spatial pattern of impervious surfaces and their impacts on land surface temperature in Beijing, China. J Environ Sci 19(2):250–256

Xiao R, Weng Q, Ouyang Z et al (2008) Land surface temperature variation and major actors in Beijing, China. Photogramm Eng Rem S 74(4):451–461

Xu YY, Liu SH, Hu F (2009) Influence of Beijing urbanization on the characteristics of atmospheric boundary layer. J Atmos Sci-ch 3(4):859–867

Yang P, Liu WD, Hou W (2011) The trend and inter-decadal evolution of extreme temperature events in Beijing area. J Catastrophology 26(1):60–64

Yu SQ, Bian LG, Lin XC (2005) Changes in the spatial scale of Beijing UHI and urban development. Sci China Ser D 48(Ⅱ):116–127

Zheng G, Lu M, Zhang T et al (2010) The impact of difference of land surface emissivity on the land surface temperature retrieval of Jinan City. J ShanDong JianZhu University 25(5):519–523(in Chinese)

Zhou J, Li J, Zhang LX (2009) Validation of algorithms for retrieving land surface temperature based on MODIS data; a case study in the upper reaches of Heihe River. J Glaciol Geocryology 31(2):239–246

Zhou W, Huang G, Cadenasso ML (2011) Does spatial configuration matter? Understanding the effects of land cover pattern on land surface tempeature in urban landscapes. Landscape Urban Plan 102:54–63

Zhou W, Qian Y, Li X et al (2011) Relationships between land cover and the surface urban heat island: seasonal variability and effects of spatial and thematic resolution of land cover data on predicting land surface temperatures. Landscape Ecol 29(1):153–167

Figure captions

Figure 1. The study area and the selected observation sites for ground-based land surface temperature (LST) observations using portable infrared thermometers and infrared thermal imagers and for radiation and energy fluxes. Note: Z1 is the LST observation site for urban impervious surface and green space; Z2 is the observation site for concrete surface; Z3 is the observation site for rural farmland; Z4 is the observation site for water body. S1 is the radiation and energy flux observation site for impervious surface (UIS); S2 is the radiation and energy flux observation site for urban green space (UGS); S3 is the radiation and energy flux observation site for rural farmland. The aerial images around the selected observation sites for LST are shown at the right. The images for the portable infrared thermometers and infrared thermal imagers are shown at the top.

Figure 2. Spatial distribution of land surface temperature as retrieved from MODIS products based on the recalibrated Mao et al. (2005) retrieval algorithm.

Figure 3. The illustrations of four levels of analyses for comparing land surface temperatures of various land-cover types, land-use types, and building materials and components along the urban-rural gradient.

Figure 4. Mean, maximum, and minimum land surface temperatures for different land surfaces in two time periods (i.e., morning: 11:00–11:30 am; midday: 12:30–1:00.

Figure 5. The locations for observing land surface temperatures of various urban structures and landscape components (i.e., buildings, plaza, and park) in the Maple Oasis residential area (Z1 in Figure 1) and the corresponding infrared images using infrared thermal imagers. (a) the observation range of the infrared thermal imagers (yellow boxes) and position (yellow circle); (b1), (b2), and (b3) landscape pictures of buildings, plaza, and green space, respectively. (c1)–(c9) the images obtained from infrared thermal imagers; c1, c2, and c3 show the thermal infrared images of b1, b2, and b3, respectively; c4, c5, and c6 represent impervious surfaces of buildings and plaza; c7, c8, and c9 represent the green space.

Figure 6. Land surface temperatures for different land-use types along the urban-rural gradient.

Figure 7. The relationship between land surface temperatures and elevations (top) and Normalized Difference Vegetation Index (NDVI).

Figure
Click here to download high resolution image

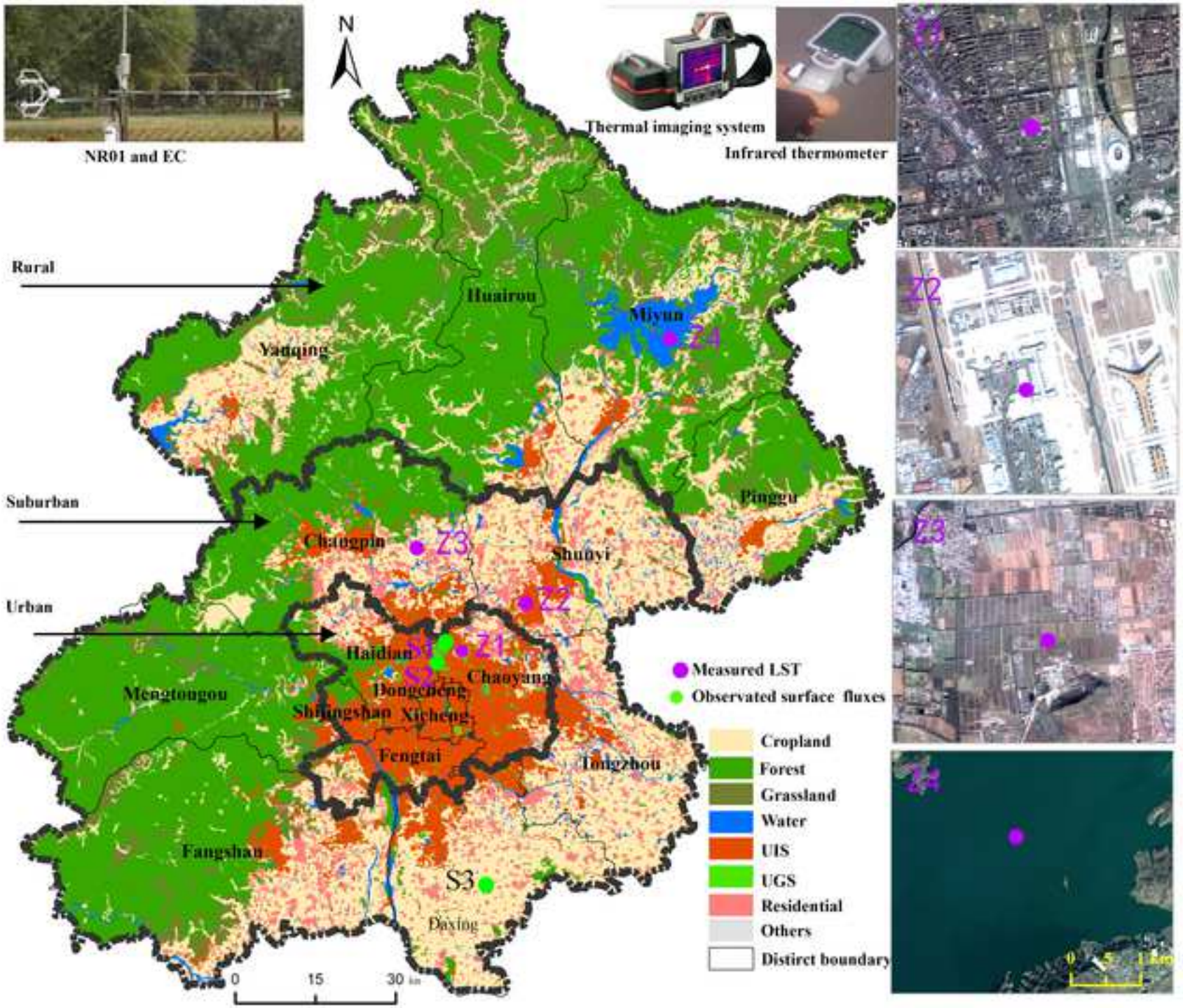

Figure
Click here to download high resolution image

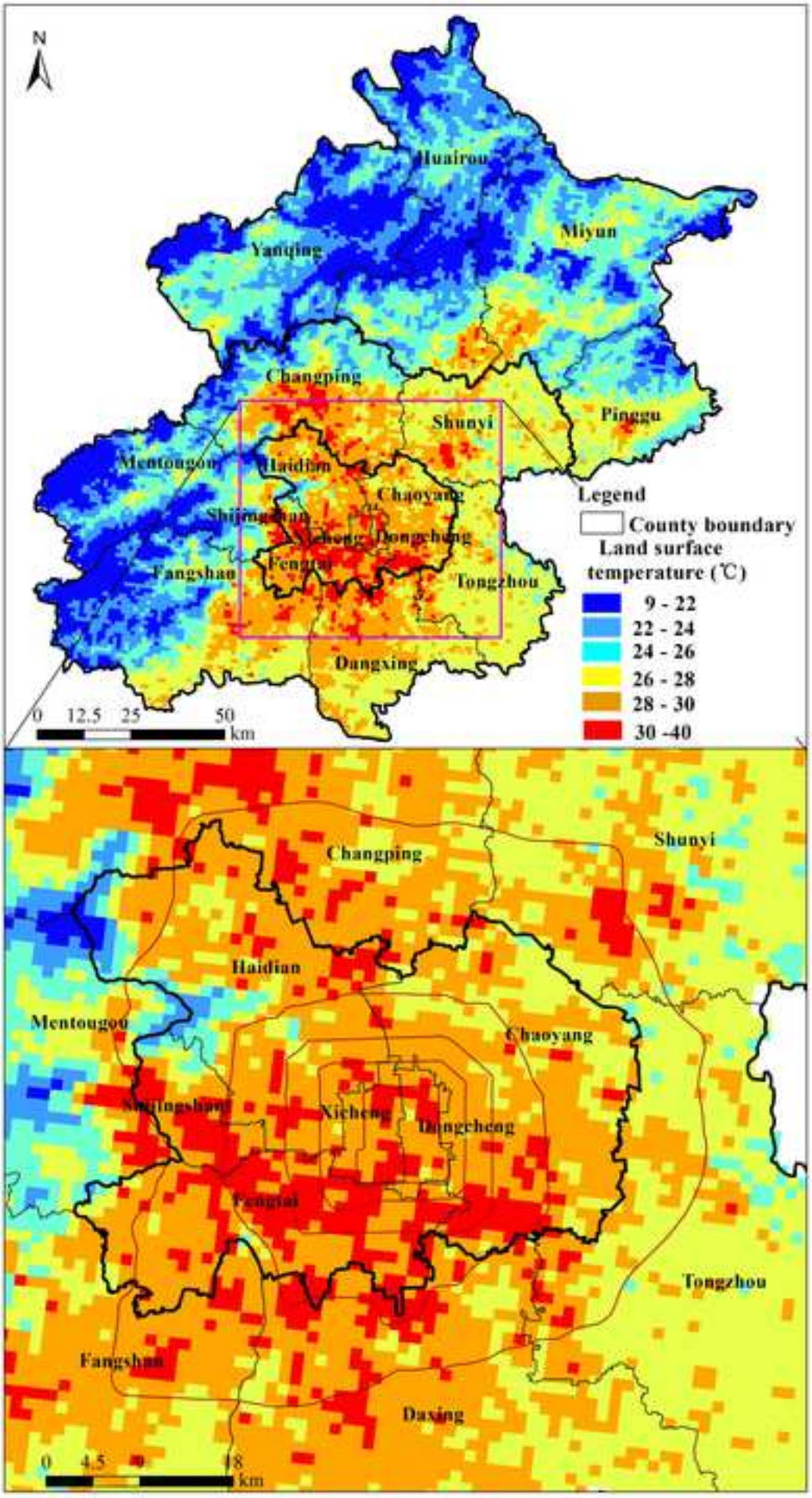

Figure

Click here to download high resolution image

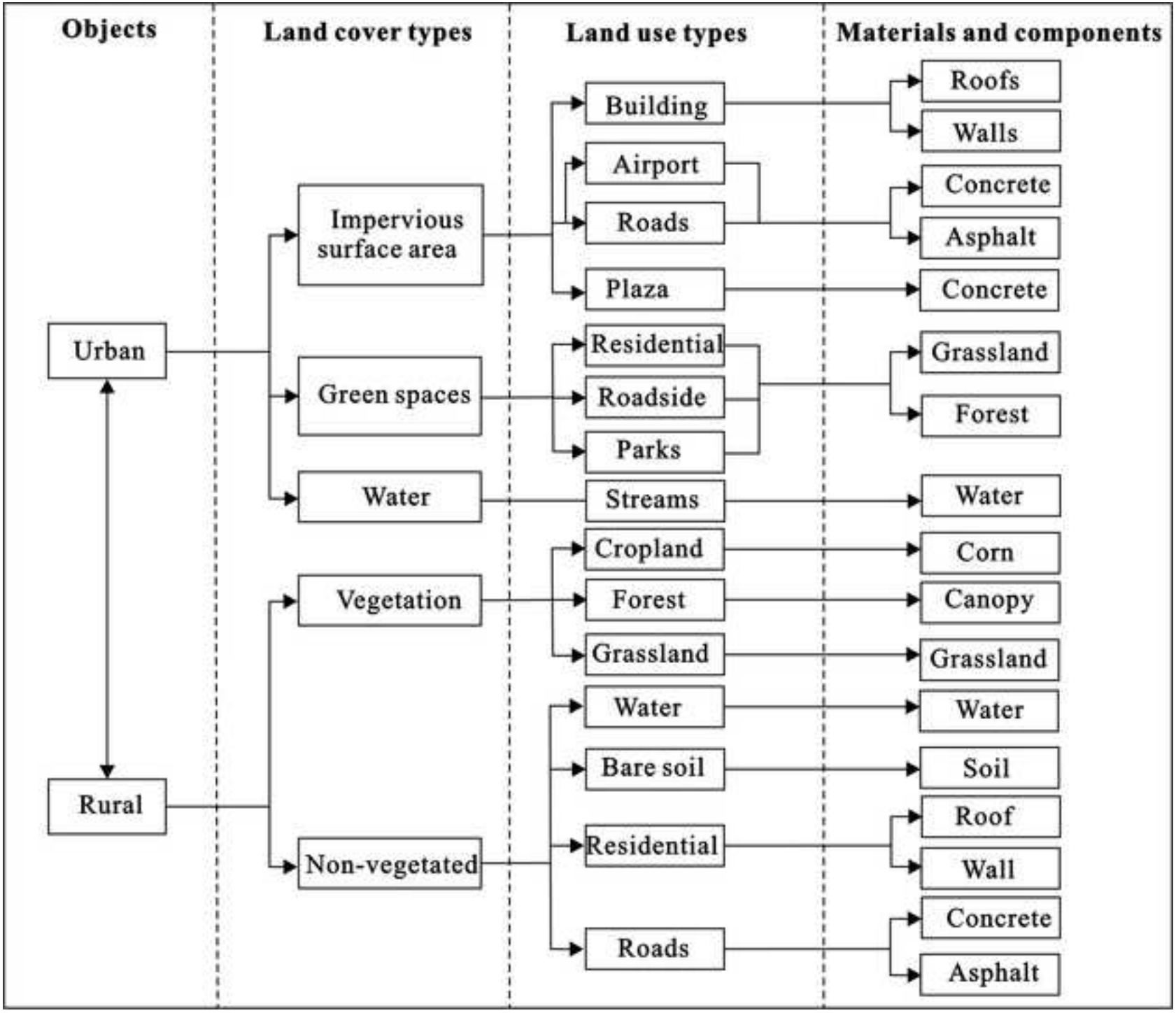

Figure
Click here to download high resolution image

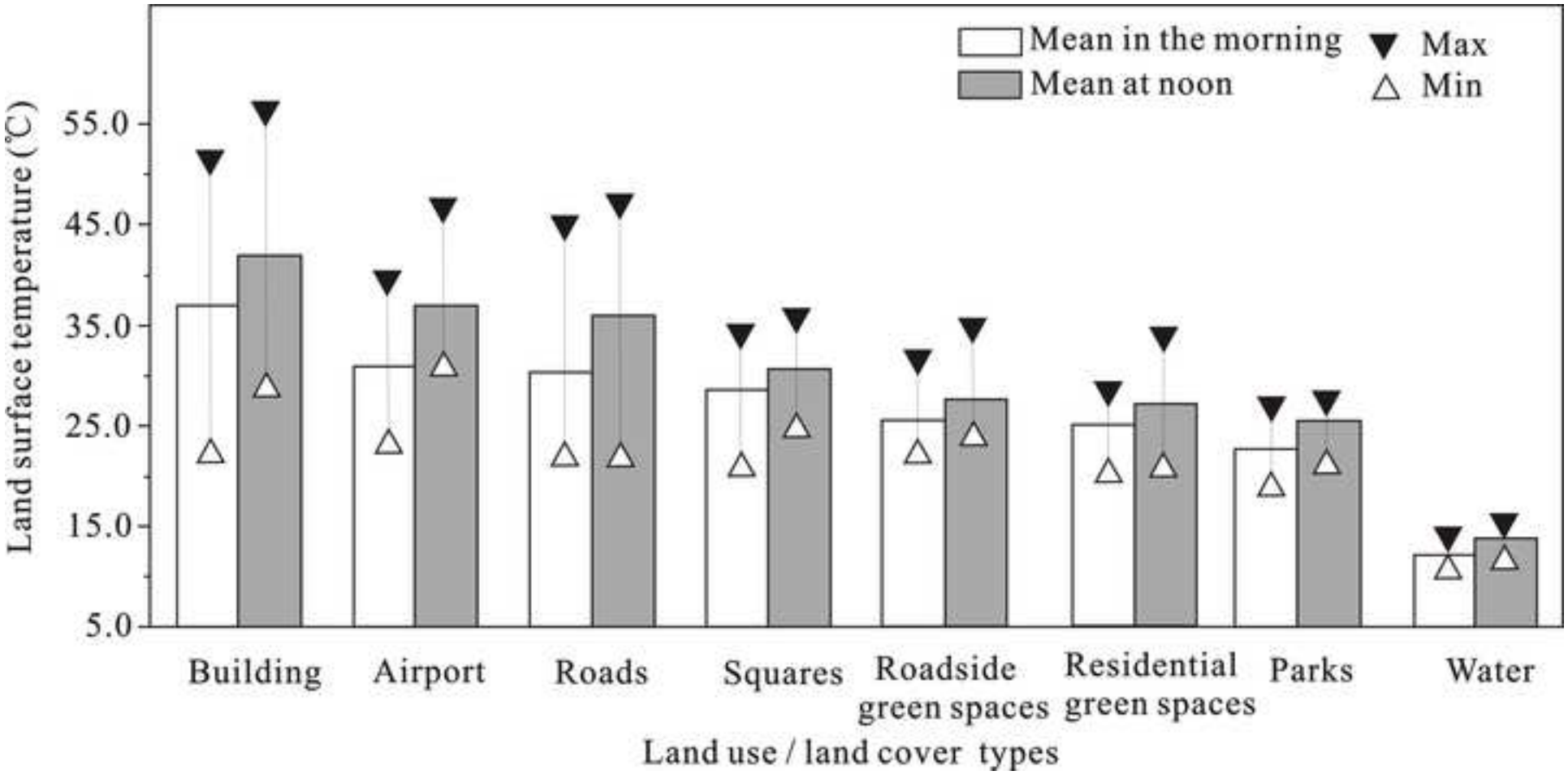

Figure

Click here to download high resolution image

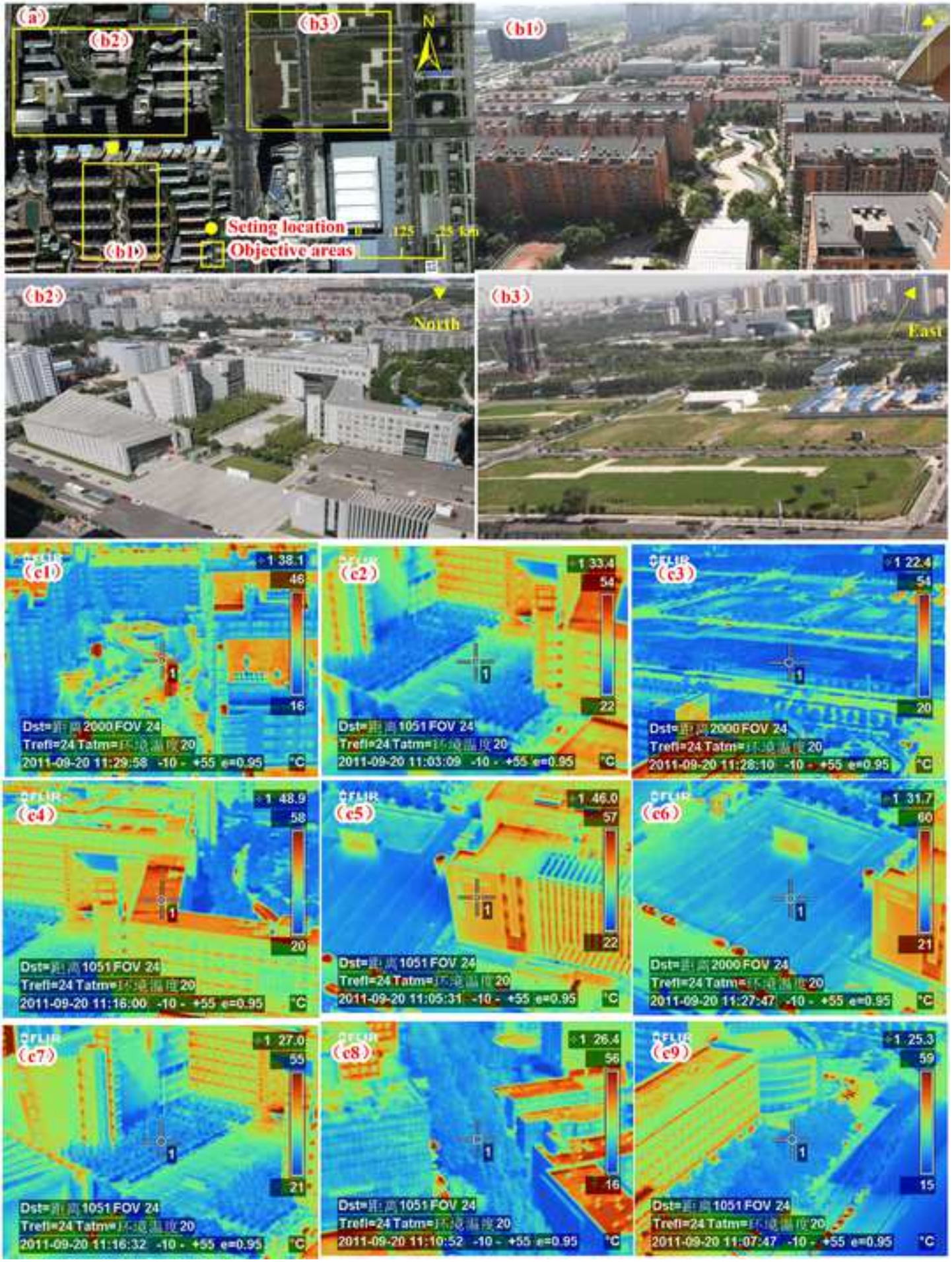

Figure
Click here to download high resolution image

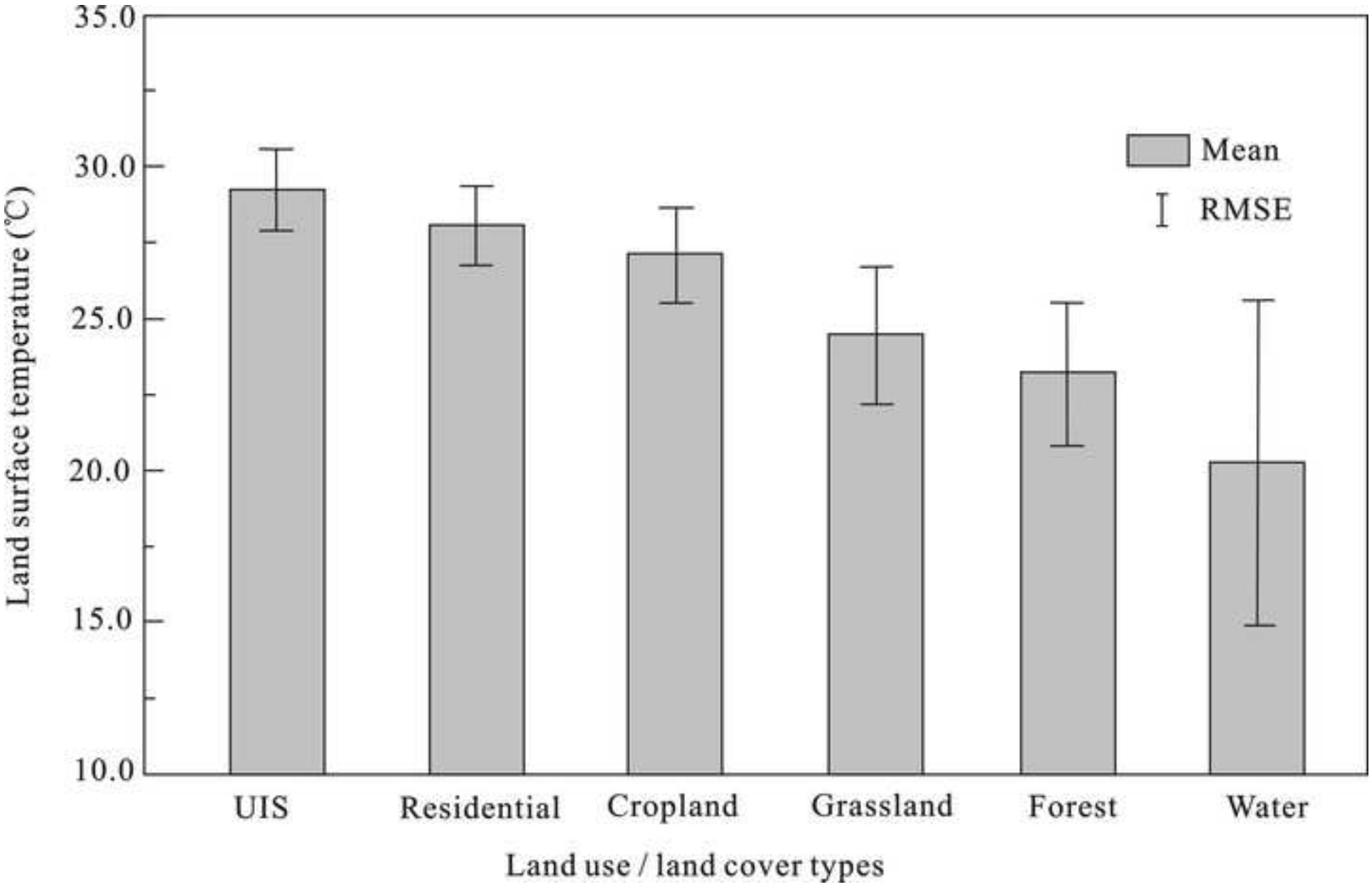

Figure
Click here to download high resolution image

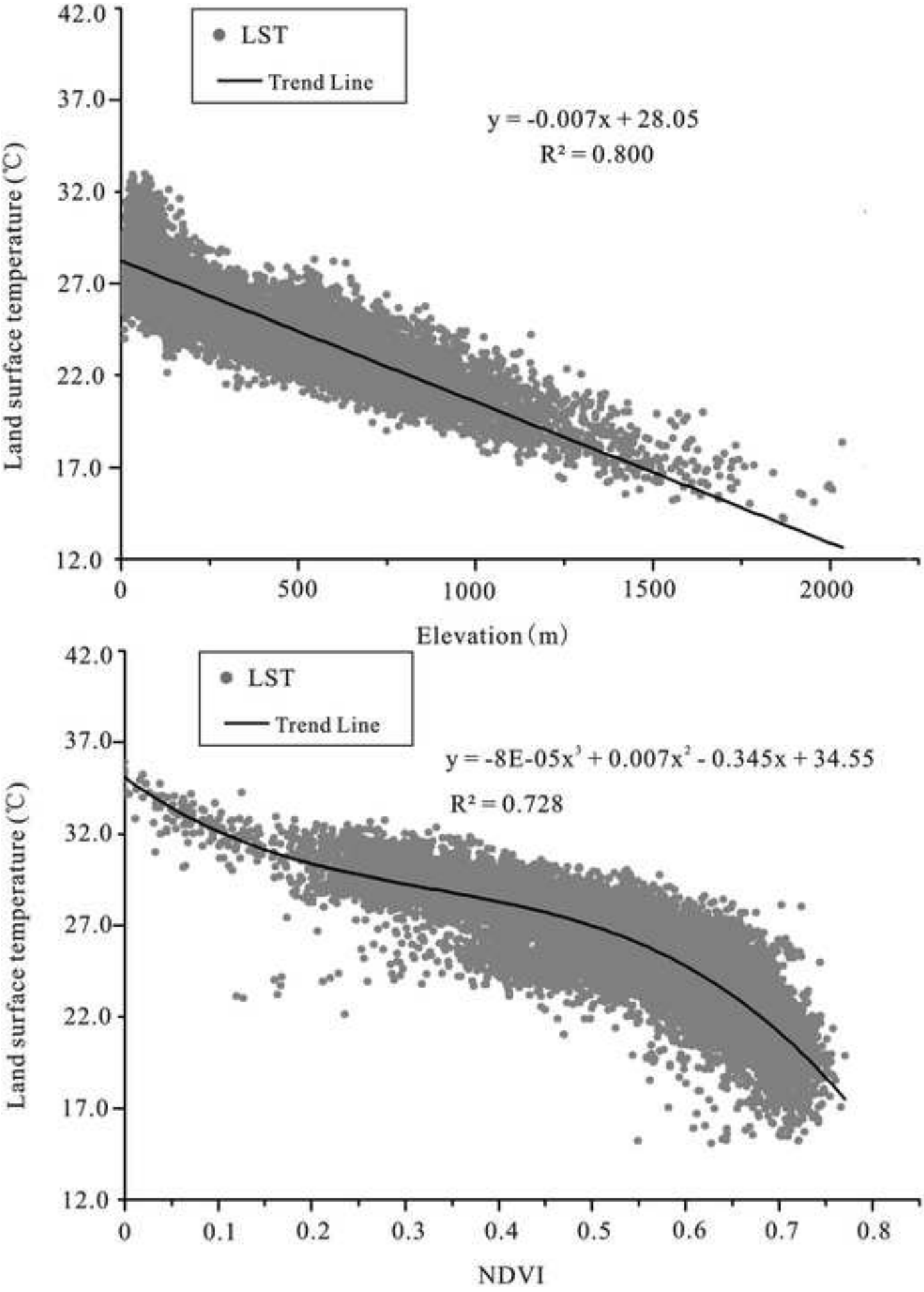

Table 1. Specific emissivity (ε_i) of different land surfaces used in this study

Land surfaces	Specific emissivity	Reference(s)
Farmland	0.982	Qin et al (2004)
Forest	0.988	Qin et al (2004)
Shrubland	0.986	Humes et al (1994); W. Liu et al (2011)
Grassland	0.982	Labed and Stoll (1991)
Water body	0.995	Zheng et al (2010)
Bare soil	0.972	Qin et al (2004)
Building	0.970	Qin et al (2004)
Green space	0.985	Humes et al (1994)
Asphalt and concrete	0.968	X. Wang et al (2011)

Table 2. Different components of solar radiation (W/m^2) during the observation periods (i.e., 11:00–11:30 AM and daytime) on September 20, 2011.

Site (land surface)	Time	Downwelling short-wave radiation	Upwelling short-wave radiation	Downwelling long-wave radiation	Upwelling long-wave radiation	Net radiation
S1 (UIS)	11:00–11:30 AM	759.29	219.47	310.79	454.54	396.07
	Daytime	409.55	119.29	303.96	443.96	262.47
S2 (UGS)	11:00–11:30 AM	777.37	142.85	330.42	472.02	492.92
	Daytime	451.85	83.12	325.79	428.73	351.87
S3 (Farmland)	11:00–11:30 AM	753.40	99.87	313.64	444.36	522.80
	Daytime	545.43	82.46	310.41	432.58	342.05

Note: UIS, urban impervious surface; UGS, urban green space.

Table 3. Land surface reflectance, net solar radiation (W/m^2), Bowen ratio, and the ratios of different heat flux components to net radiation during the observations at selected sites on September 20, 2011.

Site (land surface)	Time	Reflectance	Rn (W/m^2)	LE/Rn	H/Rn	G/Rn	Bowen Ratio (H/LE)
S1 (UIS)	11:00–11:30 AM	0.29	396.07	0.17	0.63	0.20	3.64
	Daytime	0.30	262.47	0.19	0.63	0.18	4.03
S2 (UGS)	11:00–11:30 AM	0.18	492.92	0.55	0.40	0.05	0.74
	Daytime	0.18	351.87	0.58	0.32	0.10	0.57
S3 (Farmland)	11:00–11:30 AM	0.13	522.80	0.59	0.35	0.06	0.60
	Daytime	0.14	342.05	0.63	0.30	0.07	0.46

Note: UIS, urban impervious surface; UGS, urban green space; R_n, net radiation; LE, latent heat flux; H, sensible heat flux; G, ground heat flux.